AIAA JOURNAL
Vol. 46, No. 7, July 2008

Large-Eddy Simulation of Separated Flow in a Channel with Streamwise-Periodic Constrictions

Jörg Ziefle,* Steffen Stolz,† and Leonhard Kleiser‡
ETH Zurich, 8092 Zurich, Switzerland

DOI: 10.2514/1.33891

Large-eddy simulations using the approximate-deconvolution subgrid-scale model of compressible flow in a channel with streamwise-periodic constrictions are performed at two Reynolds numbers of 2800 and 10,595. The goal of the study is the evaluation of this subgrid-scale model for massively separated flows. The Mach number was chosen as 0.2 to facilitate comparison with incompressible flow data. A relatively coarse structured grid and a finite-volume discretization employing a skew-symmetric fourth-order central scheme are used with a four-stage Runge–Kutta method for time integration. The results are compared to data from the literature obtained with incompressible direct numerical simulations, as well as highly resolved large-eddy simulations. Despite the chosen coarse resolution, good agreement of the statistical quantities and important flow features, such as separation and reattachment locations, is achieved. In contrast to previous works we also consider the flow properties at the straight upper wall. We introduce a new measure quantifying the time fraction of reverse flow along the wall. Furthermore, we analyze the energy density spectra of the velocity fluctuations and study the turbulence structure with Lumley's flatness parameter and realizability map. We also illustrate the vortex systems associated with the shedding and other instantaneous flow structures.

Nomenclature

c_f, c_p	=	friction and pressure coefficients
$E_{\cdot\cdot}$	=	power density of quantity $\cdot$
F	=	Lumley's flatness parameter
f	=	frequency
$f_{\bar{\rho}\tilde{u}}$	=	volume force in the streamwise filtered momentum equation
h	=	hill height
II, III	=	second and third Lumley invariants
L_x, L_y, L_z	=	domain size in the x, y, and z directions
Ma	=	Mach number
n	=	wall-normal direction
Pr	=	Prandtl number
p	=	pressure
R_{gas}	=	mass-specific gas constant
Re	=	Reynolds number
$\text{RHS}_{\bar{\rho}\tilde{u}}$	=	right-hand side of streamwise momentum equation
r	=	backflow fraction [Eq. (2)]
S	=	surface
St	=	Strouhal number
T	=	temperature
t	=	time
u, v, w or u_i $(i = 1, 2, 3)$	=	velocities in the x, y, and z directions
V	=	volume
x, y, z	=	streamwise, spanwise, and vertical directions
x_{sep}, x_{reatt}	=	separation and reattachment positions
γ	=	isentropic coefficient
Δt, ΔT	=	time step, time interval
Δz^+	=	wall distance in wall units
λ_2	=	vortex-identification criterion
μ	=	dynamic viscosity
ρ	=	density
τ	=	stress

Subscripts

ref	=	reference quantity
$\mathcal{S}$	=	cross-sectional bulk quantity in plane above hillcrest [i.e., $(\cdot)_{\mathcal{S}} = \int_S (\cdot)\|_{x=0} \mathrm{d}S / \int_S \mathrm{d}S$]
$\mathcal{V}$	=	volumetric bulk quantity [i.e., $(\cdot)_{\mathcal{V}} = \int_V (\cdot) \mathrm{d}V / \int_V \mathrm{d}V$], computational domain
wall	=	wall quantity
$\parallel$	=	wall-parallel vector component
$\perp$	=	wall-normal vector component

Operators

$\bar{\cdot}$	=	low-pass filtering
$\check{\cdot}$	=	derived quantity computed from low-pass filtered quantities
$\tilde{\cdot}$	=	Favre filtering
$\tilde{\cdot}'' = \tilde{\cdot} - \langle\tilde{\cdot}\rangle$	=	Favre fluctuation
$\langle\cdot\rangle$ or $\langle\cdot\rangle_t$	=	time (ensemble) averaging
$\langle\cdot\rangle_x$, $\langle\cdot\rangle_y$	=	spatial averaging in x and y directions

Presented as Paper 5353 at the 17th AIAA Computational Fluid Dynamics Conference, Toronto, Ontario, Canada, 6–9 June 2005; received 20 August 2007; accepted for publication 20 December 2007. Copyright © 2008 by the authors. Published by the American Institute of Aeronautics and Astronautics, Inc., with permission. Copies of this paper may be made for personal or internal use, on condition that the copier pay the $10.00 per-copy fee to the Copyright Clearance Center, Inc., 222 Rosewood Drive, Danvers, MA 01923; include the code 0001-1452/08 $10.00 in correspondence with the CCC.

*Ph.D. Student, Institute of Fluid Dynamics; ziefle@ifd.mavt.ethz.ch. Member AIAA.

†Research Associate, Institute of Fluid Dynamics; current address: Philip Morris International R&D, Avenue des Sports 42, Yverdon 1400, Switzerland.

‡Professor, Institute of Fluid Dynamics. Member AIAA.

I. Introduction

THE phenomenon of massive flow separation is of importance in numerous flows of industrial interest. Separation can occur at bluff bodies such as turbine blades or vehicle bodies and often leads to suboptimal operating conditions and performance deterioration. It is therefore important for computational fluid dynamics (CFD) to accurately predict separation and reattachment, as well as the flow conditions in those regions, at affordable computational cost. The numerical simulation of flows with separation from curved surfaces

is especially challenging, because the separation location is not prescribed as for sharp edges but is often spatially fluctuating in a highly spotty and unsteady manner. The separation process naturally exerts great influence on the downstream flow. Previous simulation studies of separated flows [1,2] revealed that a deviation in the prediction of the mean separation location can lead to an error nearly a decade higher in the prediction of downstream flow behavior, for example, the mean reattachment location.

Because direct numerical simulations (DNS) are feasible only for low Reynolds numbers, computationally cheaper but still accurate simulation methods have to be developed. The traditional way to reduce the computational expense in a turbulent flow simulation is to time average the Navier–Stokes equations, yielding the Reynolds-averaged Navier–Stokes (RANS) equations. The unclosed Reynolds stresses need to be modeled by a statistical turbulence model. Many different RANS models have been developed over the years, however, often an adjustment of model parameters is needed to account for the conditions of a specific flow case. A major problem for most models is the prediction of challenging flow regimes such as the laminar-turbulent transition, separation, and reattachment.

An alternative simulation methodology, which is computationally more expensive than RANS but provides much more detailed and more accurate results, is the large-eddy simulation (LES). In this approach small scales are removed by filtering the Navier–Stokes equations with a spatial low-pass filter. Thereby unclosed subgrid-scale (SGS) stresses arise which have to be modeled. In recent years, a number of different SGS models have been developed. An overview can be found in the reviews of Sagaut [3], Meneveau and Katz [4], Lesieur and Métais [5], and Domaradzki and Adams [6]. Because of its ability to accurately resolve unsteady flow processes and its (compared to DNS) relatively lower computational cost, LES is a suitable approach for the simulation of massively separated flows.

The streamwise-periodic hill channel (Fig. 1a) is one of the standard test cases for the computation of separated flows from curved surfaces. Investigations of this configuration typically serve two purposes. Direct numerical simulations and highly resolved large-eddy simulations are performed to investigate the physical flow properties due to the separation process. These results can then be used by turbulence modelers to assess and improve their turbulence models for RANS or subgrid-scale models for LES. The streamwise-periodic hill channel is well suited for such a venture. The simple geometry and clearly defined boundary conditions facilitate the reproducibility and comparability of results. Still, the standard flow conditions investigated, notably the Reynolds number and spanwise domain width, require relatively high resolution (particularly in the separation region) and long integration times for obtaining accurate statistics.

Periodic-hill flow has been extensively investigated both experimentally and numerically in the past. In contrast to the originally measured configuration [7], the interhill distance has been enlarged in the simulation studies. This allows the flow to reattach freely between the hills and recover in the postreattachment zone, while in the experiment the reattachment is forced due to the impingement of the separated flow onto the next downstream elevation of the wall. A review of RANS results can be found in [8–10]. Furthermore, large-eddy simulations were performed by several groups [1,11–15]. Because of the computational cost, direct numerical simulations for this test case have been performed only recently by Peller and Manhart [16] as well as by Breuer et al. [14] at a reduced Reynolds number. A more detailed documentation of our research of the periodic-hill channel can be found in [17]. In an extension of this study [18,19], we investigated compressibility effects on the streamwise-periodic hill channel in a series of simulations with Mach numbers increasing up to 2.5.

The aim of the work presented here is to evaluate the approximate-deconvolution subgrid-scale model (ADM) [20–22] for LES of unsteady separated flows. ADM has been demonstrated to work well in past studies [21–31] for incompressible and compressible flows, in conjunction with various numerical methods and in a broad range of transitional and turbulent flow scenarios. By comparing our results with high-resolution LES and DNS data, we also demonstrate the capability of LES to yield high-quality results at relatively coarse resolution.

This paper is organized as follows. After a short presentation of the flow geometry and boundary conditions in Sec. II, we outline the employed simulation code, subgrid-scale model, numerical method, simulation parameters, and spatial discretization in Sec. III. In Sec. IV, we present our LES results and compare vertical mean-flow profiles and the friction and pressure coefficients at the walls to reference data of Peller and Manhart [16] and Breuer et al. [14]. In addition to a discussion of the mean flowfield and its associated flow features with spanwise contours of various mean-flow quantities, we investigate the frequency content of the velocity fluctuations and their dominant components with their energy density spectra. The turbulence structure is studied in detail with Lumley's flatness parameter and anisotropy invariance triangle [32]. We highlight some typical vortical structures appearing in the instantaneous flow and describe their interaction. Finally, we illustrate the characteristics of the instantaneous separation process by introducing a new measure which quantifies the temporal fraction of reverse flow at the walls.

II. Flow Configuration

Figure 1a shows a side view of the streamwise-periodic hill channel flow configuration. At the bottom and top, the channel is constrained by solid walls. Periodic boundary conditions are employed in the streamwise (x) and spanwise (y) directions. The hill height h is chosen as the reference length for nondimensionalization, and henceforth omitted for brevity. The computational box extends over $L_x = 9$ in the streamwise direction, $L_z = 3.036$ in the wall-normal direction, and $L_y = 4.5$ in the spanwise direction.

Although the structure of the mean flowfield depends on the specific flow conditions, the flow typically separates in a highly unsteady manner shortly behind the hilltop and reattaches somewhere in the flat region between the hills. The resulting separation bubble can be recognized only in the mean flowfield. The instantaneous flow shows a periodic shedding of smaller vortices that are convected downstream. These highly unsteady flow properties, which are discussed at the end of this paper, lead to long sampling times (about 40–50 flow-through times) to obtain sufficiently converged statistics.

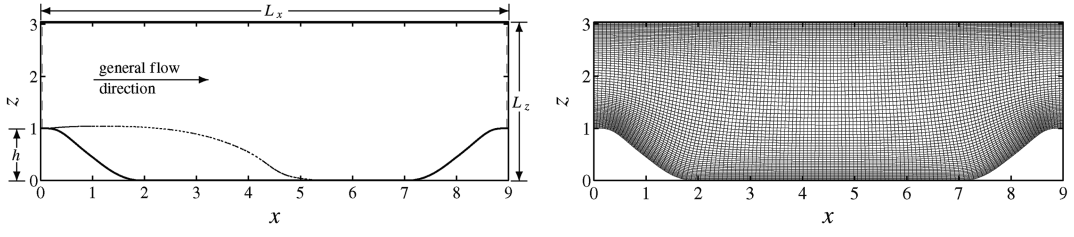

Fig. 1 a) Sketch of the periodic-hill channel (dotted line: edge of the mean-flow recirculation zone with clockwise orientation) and b) present computational mesh.

III. Numerical Method, SGS Model, and Flow Parameters

The Navier–Stokes multiblock (NSMB) code [33,34] employed for this study is a block-parallel cell-centered compressible finite-volume solver for structured grids. NSMB incorporates a number of different RANS and LES models, as well as numerical (central and upwind) schemes with an accuracy up to fourth order (fifth order for upwind schemes). Technical details about NSMB can be found in [35], and examples of complex flows simulated with NSMB are published in [30,31,36–38].

The main components of the ADM, which is employed here as a subgrid-scale model, are the direct computation of the nonlinear fluxes with an approximation of the unfiltered state vector, obtained by an approximate-deconvolution (defiltering) procedure [20], and a relaxation term employed for regularization [22]. The approximate deconvolution is based on a truncated series expansion of the inverse LES filter, leading to an approximate-deconvolution filter defined by a linear combination of the repeatedly filtered state vector.

In our computations, filtering is carried out with an explicit discrete graded filter with Fourier transform $\hat{G}$ in a general formulation for structured curvilinear grids [21]. For the inner points away from the walls, the filter consists of a central five-point stencil with a commutation error of third order (i.e., polynomials of up to second order are invariant to filtering). The filter cutoff wave number ω_c, defined by $|\hat{G}(\omega_c)| = 1/2$, is located at $\omega_c \approx 2\pi/3$. Near the walls asymmetric stencils with similar properties are employed for consistency. The deconvolution order [20] is set to the well-proven value of 5, leading to a good approximate reconstruction of the unfiltered quantities from the filtered ones [39]. In favor of a reduced computational cost and memory usage, we employed constant relaxation coefficients χ in the relaxation terms for the continuity, momentum, and energy equations. This simplification is justified by previous studies [21,26] which revealed a low sensitivity of the results to the value of the relaxation coefficient. In contrast to previous compressible ADM simulations [22–24,27–29], the mass loss resulting from the introduction of the relaxation term into the continuity equation was counteracted by a forcing term similar to the one described below for the streamwise momentum equation.

Past work of our group using NSMB has focused on the evaluation and validation of the ADM subgrid-scale model in conjunction with the finite-volume approach in simple (single-block) geometries such as supersonic channel [27,28] and compression-ramp [29] flows. In the course of the recent work, a flexible and multiblock-capable block-parallelized version of the ADM subgrid-scale model for general geometries and boundary conditions has been implemented into NSMB. However, by virtue of the rather simple topology of the periodic-hill channel, all calculations presented herein could be performed on a single block.

The flow is driven by a forcing term representing a mean pressure gradient, which is implemented as a spatially constant but temporally varying volume force in the streamwise direction. To obtain a constant volume-integrated streamwise momentum $\int_{\mathcal{V}} \bar{\rho}\,\tilde{u}\ \mathrm{d}V$ (i.e., the condition $\partial \int_{\mathcal{V}} \bar{\rho}\,\tilde{u}\ \mathrm{d}V/\partial t \equiv 0$), this volume force $f_{\bar{\rho}\tilde{u}}(t)$ is added to the right-hand side of the streamwise momentum equation $\mathrm{RHS}_{\bar{\rho}\tilde{u}}$ and integrated over the computational domain $\mathcal{V}$,

$$\frac{\partial}{\partial t}\int_{\mathcal{V}} \bar{\rho}\,\tilde{u}\ \mathrm{d}V = \int_{\mathcal{V}} \mathrm{RHS}_{\bar{\rho}\tilde{u}}(t)\,\mathrm{d}V + f_{\bar{\rho}\tilde{u}}(t)\int_{\mathcal{V}} \mathrm{d}V \equiv 0 \qquad (1)$$

From Eq. (1) the volume force $f_{\bar{\rho}\tilde{u}}(t)$ can be computed at each time step. In finite-volume codes, volume integration can be performed exactly as the sum of the cell integrals. Therefore, the volume-integrated streamwise momentum $\int_{\mathcal{V}} \bar{\rho}\,\tilde{u}\ \mathrm{d}V$ can be fixed within machine accuracy. Note that the forcing also enters the energy equation in the form of a term $f_{\bar{\rho}\tilde{u}}\tilde{u}$, with $\tilde{u}$ being the Favre-filtered streamwise velocity. Although the volumetric Reynolds number

$$Re_{\mathcal{V}} := \int_{\mathcal{V}} \bar{\rho}\,\tilde{u}\ \mathrm{d}V h \Big/ \left(\int_{\mathcal{V}} \mathrm{d}V \check{\mu}_{\mathrm{wall}}\right)$$

is kept constant by the forcing, the cross-sectional Reynolds number over the hillcrest

$$Re_{\mathcal{S}} := \int_{\mathcal{S}} (\bar{\rho}\,\tilde{u})\Big|_{x=0} \mathrm{d}S\, h \Big/ \left(\int_{\mathcal{S}} \mathrm{d}S \check{\mu}_{\mathrm{wall}}\right)$$

(see Fig. 2a) is a function of time and fluctuates slightly, due to mass flux variations in the cross section over the hillcrest, around the mean value of $\langle Re_{\mathcal{S}}\rangle = Re_{\mathcal{V}}/\Gamma$, with Γ denoting the geometry factor

$$\Gamma := L_x L_z(x=0) \Big/ \int_{x=0}^{L_x} L_z(x)\,\mathrm{d}x \approx 0.72$$

Also depicted in Fig. 2b is the magnitude of the forcing term for the streamwise momentum equation $f_{\bar{\rho}\tilde{u}}(t)$.

To allow for a comparison of the results with incompressible reference data, the Mach number $Ma := \tilde{u}_{\mathcal{V}}/\sqrt{\gamma R_{\mathrm{gas}} \check{T}_{\mathrm{wall}}}$ is set to the low value of 0.2, yielding a maximum local average Mach number of $\langle Ma_{\mathrm{local,max}}\rangle \approx 0.27$. A perfect gas with an isentropic coefficient of $\gamma = 1.4$ is considered. The no-slip walls are assumed to be isothermal, and the dependency of the dynamic viscosity on the temperature is modeled with a power law [40], $\check{\mu}(\check{T})/\check{\mu}_{\mathrm{wall}} = (\check{T}/\check{T}_{\mathrm{wall}})^{0.7}$. Additionally, a vanishing wall-normal pressure gradient $\partial \check{p}/\partial n = 0$ is enforced at the walls.

The computational grid used for the present calculations (Fig. 1b) was generated with the commercial mesh generator GridPro [41]. It uses 128 cells in the streamwise direction. For an accurate prediction of the mean separation point, which itself greatly influences the size and extent of the recirculation zone [1], a minimum resolution particularly in the streamwise direction of about this number is necessary. The spanwise direction is discretized with 72 cells, while in the wall-normal direction 69 cells are employed. The grid stretching and resolution at both walls is comparable, with a stretching factor of well below 1.1. The mean distance in wall units of the first cell off the upper wall is $\langle \Delta z^+\rangle_x \approx 2.16$ for a Reynolds number of $\langle Re_{\mathcal{S}}\rangle \approx 10,595$ ($\langle \Delta z^+\rangle_x \approx 0.78$ for $\langle Re_{\mathcal{S}}\rangle \approx 2800$) with a maxima of $\Delta z^+_{\max} \approx 2.70$ for $\langle Re_{\mathcal{S}}\rangle \approx 10,595$ and $\Delta z^+_{\max} \approx 1.01$

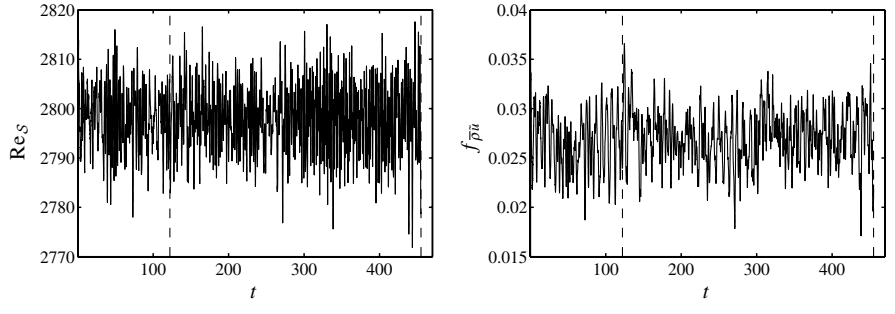

Fig. 2 Temporal development of a) cross-sectional bulk Reynolds number $Re_{\mathcal{S}}$ and b) forcing term in the streamwise momentum equation $f_{\bar{\rho}\tilde{u}}$ ($\langle Re_{\mathcal{S}}\rangle \approx 2800$). Dashed lines: bounds of statistical averaging period.

Table 1 Calculation parameters, mesh dimensions, and separation/reattachment locations of the present and reference simulations. The domain size is $L_x = 9$, $L_y = 4.5$, and $L_z = 3.036$ in all cases

Simulation	$\langle Re_S \rangle$	Ma	$N_x \times N_y \times N_z$	1×10^6 cells	x_{sep}	x_{reatt}
Peller & Manhart [16] (DNS)	2,800	N/A	$464 \times 304 \times 338$	47.68 ($\hat{=}$100%)	0.21	5.41
Breuer et al. [14] (DNS)	2,800	N/A	$464 \times 304 \times 338$	47.68 ($\hat{=}$100%)	0.22	5.41
Present (LES)	2,800	0.2	$128 \times 72 \times 69$	0.64 ($\hat{\approx}$1%)	0.21	5.30
Breuer et al. [14] (LES)	10,595	N/A	$280 \times 220 \times 200$	12.32 ($\hat{=}$100%)	0.19	4.69
Temmerman & Leschziner [12] (LES)	10,595	N/A	$196 \times 186 \times 128$	4.67 ($\hat{\approx}$38%)	0.22	4.72
Peller & Manhart [16] (LES)	10,595	N/A	$221 \times 106 \times 173$	4.05 ($\hat{\approx}$33%)	0.27	4.15
Present (LES)	10,595	0.2	$128 \times 72 \times 69$	0.64 ($\hat{\approx}$5%)	0.21	4.68

for $\langle Re_S \rangle \approx 2800$, respectively. Table 1 summarizes the main simulation parameters and compares the presently used grid resolution to the much finer ones used in the reference simulations.

The simulations of the present study are carried out with a skew-symmetric central scheme of fourth-order accuracy, whose intrinsic properties contribute to accuracy and numerical stability by reducing aliasing errors [42]. The Navier–Stokes equations are integrated in time with a standard four-stage Runge–Kutta scheme. The time step is held constant at $\Delta t = 10^{-3}$ in time units $h/\tilde{u}_V$, corresponding to a CFL number of approximately 1 (i.e., about one-third of the linear stability limit of the time-integration scheme). Statistical samples are accumulated by spanwise and time averaging over a period of more than 50 flow-through times $L_x/\tilde{u}_V$. The simulations consumed about 400 CPU hours each on a single processor of a NEC SX-5 vector computer.

IV. Results

In the following, our LES results at a Reynolds number of $\langle Re_S \rangle \approx 2800$ will be presented and compared to recent DNS data from literature. Breuer et al. [14] used a second-order finite-volume discretization of the incompressible Navier–Stokes equations on a curvilinear mesh. Peller and Manhart [16] employed an immersed boundary technique on a nonequidistant staggered Cartesian mesh in conjunction with an incompressible second-order finite-volume solver. Their mesh consisted of $464 \times 304 \times 338$ cells, of which 91% were located within the computational domain. The maximum distance in wall units of the first cell above the wall is $\Delta z^+ \approx 1.4$ near the hillcrest, with significantly lower values occurring along the rest of both walls. Furthermore, we also present our results for the higher Reynolds number $\langle Re_S \rangle \approx 10595$, for which high-resolution incompressible LES data (using the wall-adapting local eddy-viscosity model [43]) from Temmerman and Leschziner [12] as well as the former two groups are available. However, due to the existence of accurate DNS data, we focus on the lower Reynolds number of $\langle Re_S \rangle \approx 2800$ in this paper.

To evaluate the influence of the SGS model, we also performed so-called "no-model" simulations, that is, simulations with switched-off subgrid-scale models on the same grid as used for the LES. Because of the lack of sufficient numerical dissipation in the fourth-order central discretization scheme of the Euler fluxes, the no-model simulations aborted due to numerical instabilities after several hundred time steps. We were able to conduct computations without an SGS model by using artificial numerical dissipation with tuned coefficients for the second- and fourth-order damping terms. However, these results (not shown here) were found to be less accurate than those of our ADM simulations, at an only slightly reduced computational cost. More important, the disadvantage of such an "implicit LES"-like (ILES) approach [44] is the need for an ad hoc adaptation of the dissipation coefficients. Our previous studies [27] revealed a rather strong dependence of the results on the specific choice of the artificial dissipation parameters.

A. Mean Stream Function

Figure 3 shows the stream-function contours of the mean velocity field together with 10 vertical profiles of the mean streamwise velocity for the Reynolds number $\langle Re_S \rangle \approx 2800$. From these 10 streamwise positions, five characteristic stations were selected for a more detailed comparison of the mean quantities and Reynolds stresses in Sec. IV.C. The velocities are normalized by the mean streamwise bulk momentum over the hillcrest $\tilde{u}_{ref} := \langle \tilde{u}_S \rangle$, and the Reynolds stresses and turbulent kinetic energy are normalized similarly by $\check{\tau}_{ref} := \langle \bar{\rho}_S \rangle \tilde{u}_{ref}^2$.

In our simulation at $\langle Re_S \rangle \approx 2800$, the flow separates at $x_{sep} \approx 0.21$ and reattaches at $x_{reatt} \approx 5.30$. This is in quite close agreement with the DNS, where the separation and reattachment points are located at $x_{sep} \approx 0.21$–0.22 and $x_{reatt} \approx 5.41$, respectively, especially when considering our coarse spatial resolution in the separation ($\Delta x_{sep} \approx 0.04$) and reattachment ($\Delta x_{reatt} \approx 0.07$) regions. Besides the large recirculation zone, we observe two much smaller separation bubbles. One is located at the foot of the windward side of the hill ($6.9 \lesssim x \lesssim 7.4$). The other one is contained within the primary separation zone at the leeward side of the hill ($0.5 \lesssim x \lesssim 0.9$). Although the former two separation bubbles also occur in the incompressible reference calculations [16], the latter recirculation zone is only observed in our results.

B. Mean Friction and Pressure Coefficients

The mean friction coefficient $\langle c_f \rangle := 2\langle \check{\tau}_w \rangle / \check{\tau}_{ref}$ at the lower wall (with the reference stress $\check{\tau}_{ref} := \langle \bar{\rho}_S \rangle \langle \tilde{u}_S \rangle^2$) in Fig. 4a shows an initial drop to negative values after separation. At $x \approx 0.3$ it rises again and nearly vanishes in the DNS, while in our LES it becomes slightly positive. The reattachment of our LES at $x \approx 5.30$ is slightly premature in comparison to the DNS (at $x \approx 5.41$), while the windward separation bubble and the following peak due to the flow acceleration are represented very well. The mean pressure coefficient $\langle c_p \rangle := (\check{p} - \langle \check{p} \rangle_x)/\check{p}_{ref}$ with the reference pressure $\check{p}_{ref} := 1/\gamma \mathrm{Ma}^2$ (for comparison, all pressure curves were moved along their ordinate so that their mean values vanish) in Fig. 4b exhibits good overall agreement between the LES and DNS. We attribute the minor deviations, for example, the slight pressure overshoot in the region $4 \lesssim x \lesssim 8$, to compressibility. Although the mean density is rather uniform in most of the computational domain, it increases by as much as 7% in a small near-wall layer along the postreattachment flow-recovery zone (cf. Fig. 9c). As the temperature in this region is almost unity due to the proximity of the isothermal wall, the near-wall pressure rises nearly proportionally to density by virtue of the ideal gas law. In conjunction with the above "rescaling" of the pressure, this causes the pressure coefficient for $0 \lesssim x \lesssim 3.5$, where very little compressibility effects can be observed, to be slightly lower than in the reference simulation. Note that discretization errors (e.g., due to the coarse grid) or (subgrid-scale) modeling errors could be additional sources for the small deviations of the pressure coefficient. Neither possibility can be completely excluded without further investigations, which would require additional (computationally expensive) simulations at a lower Mach number and a higher spatial resolution.

In Figs. 4c and 4d, the corresponding distributions of the friction and pressure coefficients are shown for the higher Reynolds number $\langle Re_S \rangle \approx 10,595$. Because the pressure field is not strongly affected by the fluid viscosity (and thus the Reynolds number), the curves of the pressure coefficient are almost the same for both Reynolds numbers. Notable changes of the pressure coefficient occur in the case of higher flow compressibility, which is dependent on the

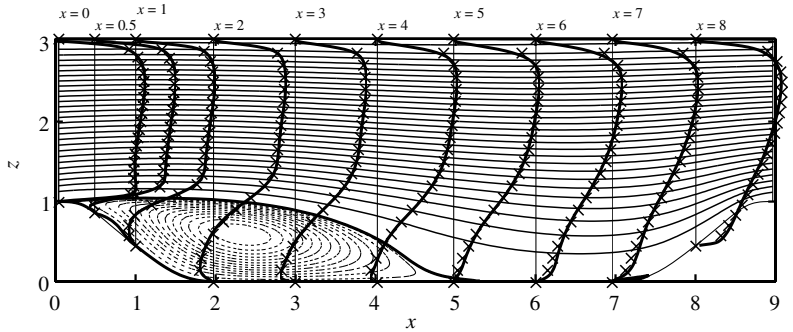

Fig. 3 Stream-function contours of the average velocity field and mean streamwise velocity profiles at 10 streamwise positions ($\langle Re_S \rangle \approx 2800$). Positive stream-function values appear as solid contour lines and negative values as dashed contour lines. Thick solid lines: edges of mean-flow recirculation zones. Solid lines: present LES, ×DNS by Peller and Manhart [16].

Mach number. In our extension study to the present work [18,19], we investigate the effects of compressibility on the streamwise-periodic hill flow in detail by varying the Mach number from 0.2 to 2.5.

Although the general appearance of the friction coefficient is quite similar to the result at $\langle Re_S \rangle \approx 2800$, there are some minor differences. The lower fluid viscosity that comes along with the higher Reynolds number causes lower values of the friction coefficient for $\langle Re_S \rangle \approx 10,595$. Furthermore, the reattachment occurs earlier, at $x \approx 4.7$.

C. Mean and Fluctuating Velocity Profiles

In Fig. 5, the mean-flow profiles for $\langle Re_S \rangle \approx 2800$ are compared at five streamwise positions, indicated by vertical lines in Fig. 3. The mean streamwise velocities $\langle \tilde{u} \rangle / \tilde{u}_{\text{ref}}$ show excellent agreement with the DNS. For the wall-normal velocity component $\langle \tilde{w} \rangle / \tilde{u}_{\text{ref}}$, the peak velocities over the hillcrest (positions $x = 0$ and $x = 8$) are slightly higher than in the reference data (note the different scale). The normalized Reynolds stresses $\langle \bar{\rho} \tilde{u}_i'' \tilde{u}_j'' \rangle / \check{\tau}_{\text{ref}}$ (computed from the Favre fluctuations $\tilde{u}_i'' = \tilde{u}_i - \langle \tilde{u}_i \rangle$) shown in Fig. 6 are in good agreement for most positions. Notable deviations occur for the streamwise stresses $\langle \bar{\rho} \tilde{u}'' \tilde{u}'' \rangle / \check{\tau}_{\text{ref}}$ in the flat region between the hills near the lower wall (positions $x = 2$ and $x = 4$), where the stresses are overpredicted. The peaks of the shear stresses $\langle \bar{\rho} \tilde{u}'' \tilde{w}'' \rangle / \check{\tau}_{\text{ref}}$ are also slightly higher in our LES.

The fact that results obtained with a second-order discretization (not shown here, see [30]) are significantly worse than the fourth-order data suggests that our coarse resolution is at the lower limit for this configuration and flow conditions. The chosen low resolution causes discretization errors to be significant, which becomes visible in the sensitive second-order statistics. This is supported by the degradation of results (not shown here) obtained with a grid using only two-thirds of the number of cells per direction at a Reynolds number of $\langle Re_S \rangle \approx 10,595$. Because of a large deviation in the prediction of the mean separation location ($x_{\text{sep}} \approx 0.59$), the reattachment occurred far too early ($x_{\text{reatt}} \approx 3.30$). For the lower Reynolds number, the results on the coarsened grid did not degrade as much but exhibited the same tendency.

On our standard grid and at the higher Reynolds number of $\langle Re_S \rangle \approx 10,595$, we observe similarly good agreement between our LES and the highly resolved LES data from literature. The mean-flow profiles displayed in Fig. 7 agree well. Slight deviations in the streamwise velocity $\langle \tilde{u} \rangle / \tilde{u}_{\text{ref}}$ are visible near the upper wall. For

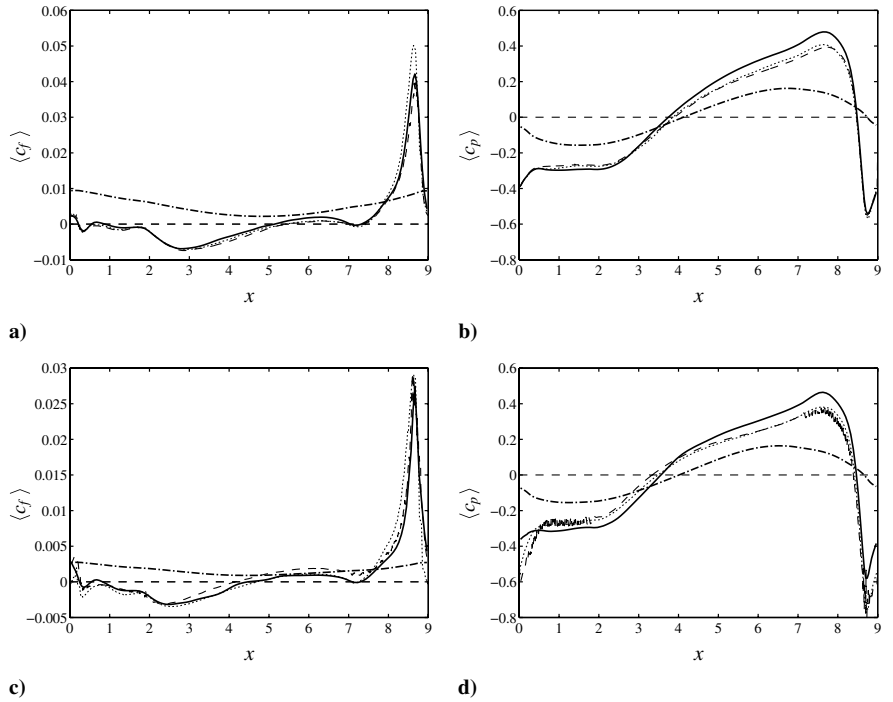

Fig. 4 a), c) Mean friction coefficient $\langle c_f \rangle$ and b), d) mean pressure coefficient $\langle c_p \rangle$ at the walls for a), b) $\langle Re_S \rangle \approx 2800$ and c), d) $\langle Re_S \rangle \approx 10,595$. Solid lines: present LES (bottom wall); dash-dotted lines: present LES (top wall); dashed lines: DNS/LES by Peller and Manhart [16]; dotted lines: DNS/LES by Breuer et al. [14].

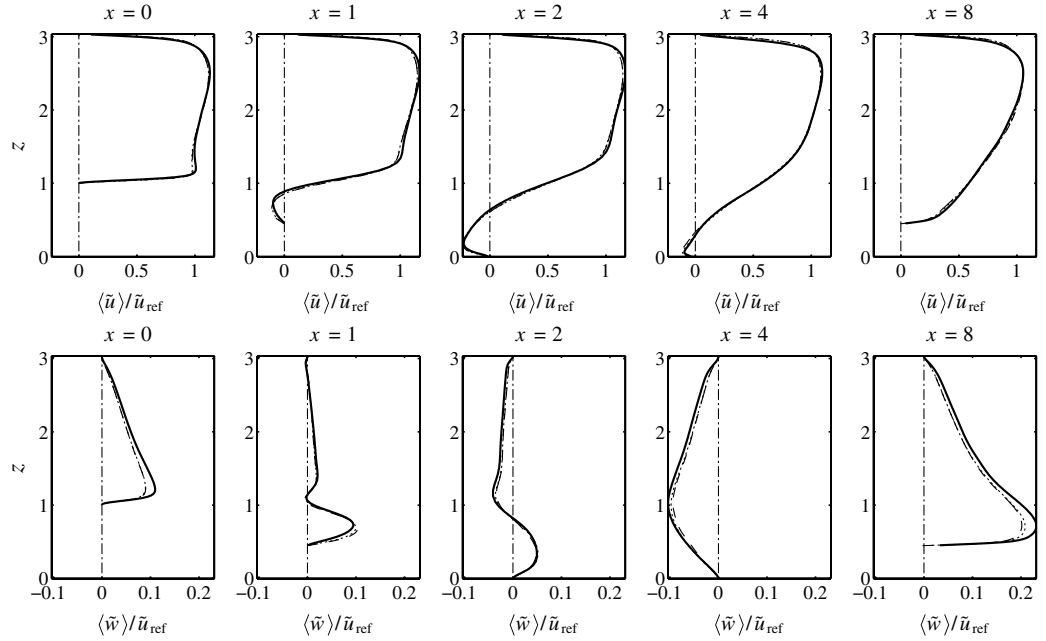

Fig. 5 Profiles of the normalized mean streamwise velocity $\langle\tilde{u}\rangle/\tilde{u}_{\mathrm{ref}}$ (top row) and the normalized mean wall-normal velocity $\langle\tilde{w}\rangle/\tilde{u}_{\mathrm{ref}}$ (bottom row) at five streamwise locations ($\langle Re_S\rangle \approx 2800$). Solid lines: present LES; dashed lines: DNS by Peller and Manhart [16]; dotted lines: DNS by Breuer et al. [14].

the wall-normal velocity $\langle\tilde{w}\rangle/\tilde{u}_{\mathrm{ref}}$, the peak near the lower wall on the hilltop ($x = 0$) is larger in our LES. The Reynolds stresses $\langle\bar{\rho}\tilde{u}_i''\tilde{u}_j''\rangle/\check{\tau}_{\mathrm{ref}}$ in Fig. 8 also correlate relatively well at most positions. However, as for the lower Reynolds number, we again observe higher streamwise velocity fluctuations $\langle\bar{\rho}\tilde{u}''\tilde{u}''\rangle/\check{\tau}_{\mathrm{ref}}$ near the lower wall in the postreattachment recovery region. Furthermore, the Reynolds-stress peaks are generally higher in our LES.

D. Contours of the Spanwise-Averaged Data

The contours of the spanwise- and temporally averaged flowfield in Fig. 9 (here presented for $\langle Re_S\rangle \approx 2800$) provide a good overview of the mean-flow properties. The streamwise velocity $\langle\tilde{u}\rangle/\tilde{u}_{\mathrm{ref}}$ (Fig. 9a) exhibits the expected behavior. The highest velocities occur in the narrowest cross section over the hillcrest. However, due to the separation bubble, the region of high velocities extends well into the first half of the flat region between the hills. This indicates that the deceleration occurs over a relatively large downstream stretch, whereas the acceleration at the windward hillside is confined to a short streamwise region, as confirmed by the pressure distribution in Fig. 4b. Note the inclined form of the high-velocity fluid layer over the hilltop. Because of the large acceleration on the windward side and the relatively large curvature of the hillcrest, the zone of high-velocity fluid does not follow the wall contour but is "ejected" at a small angle toward the upper wall. Also remarkable in Fig. 9a is a horizontal layering of the streamwise velocity. After $x \approx 5.5$ the low-velocity zone thins out significantly over a short streamwise stretch, which is caused by the flow recovery after reattachment. The lowest streamwise velocities naturally occur in the main separation region. Also note the thickening of the boundary layer at the upper wall between $x \approx 3$ and $x \approx 6$ due to the presence of an adverse pressure gradient, which is also visible in the pressure contours in Fig. 9d.

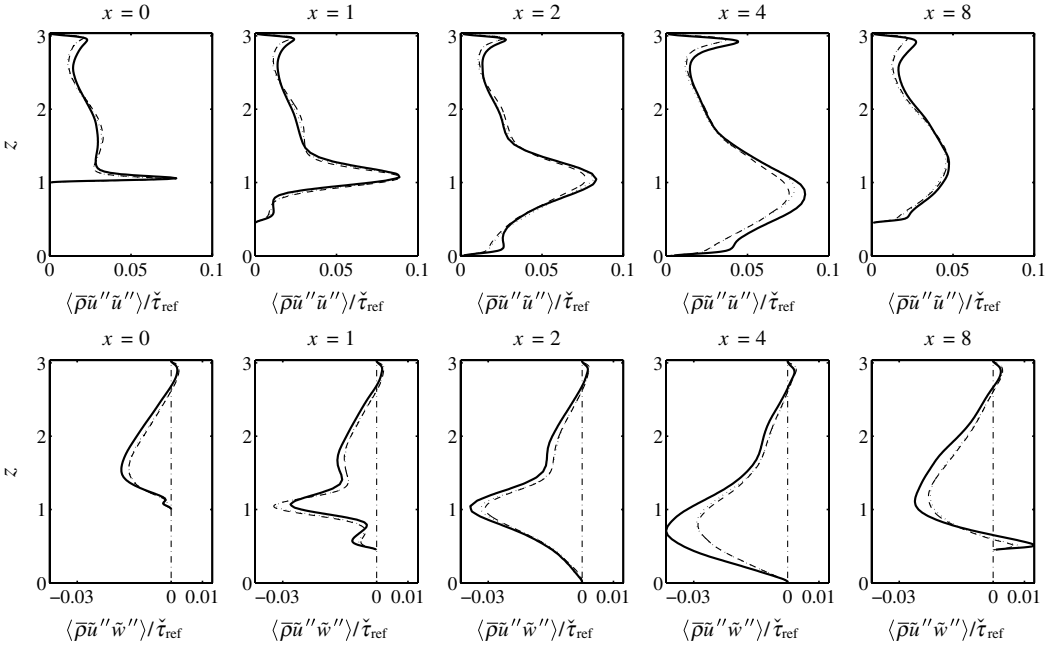

Fig. 6 Profiles of the normalized Reynolds stresses $\langle\bar{\rho}\tilde{u}''\tilde{u}''\rangle/\check{\tau}_{\mathrm{ref}}$ (top row) and $\langle\bar{\rho}\tilde{u}''\tilde{w}''\rangle/\check{\tau}_{\mathrm{ref}}$ (bottom row) at five streamwise locations ($\langle Re_S\rangle \approx 2800$). Solid lines: present LES; dashed lines: DNS by Peller and Manhart [16]; dotted lines: DNS by Breuer et al. [14]

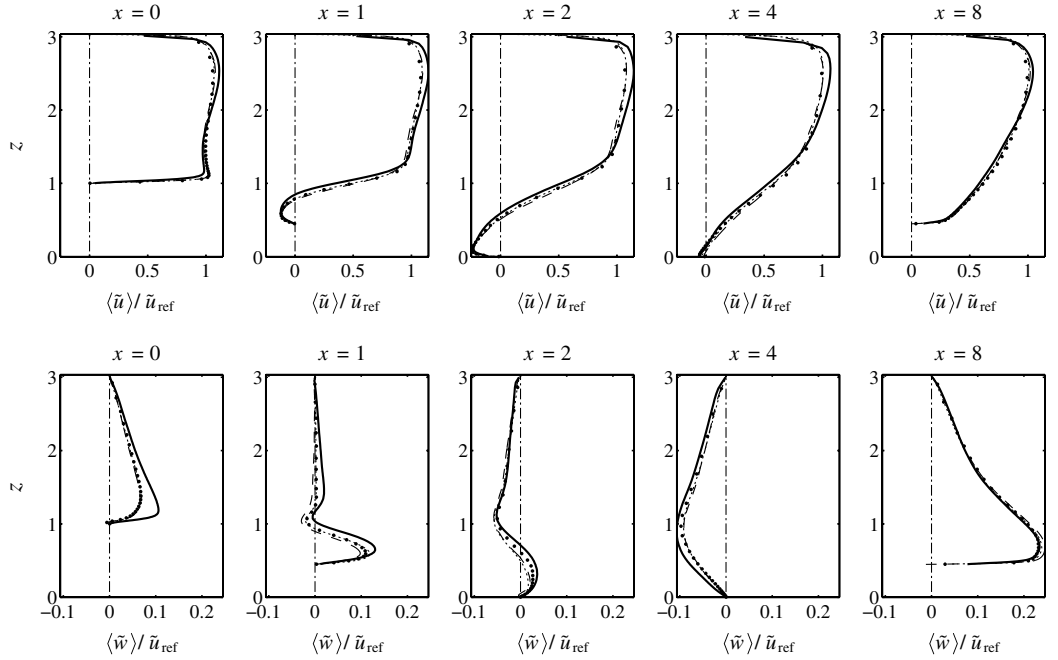

Fig. 7 Profiles of the normalized mean streamwise velocity $\langle\tilde{u}\rangle/\tilde{u}_{\mathrm{ref}}$ (top row) and normalized mean wall-normal velocity $\langle\tilde{w}\rangle/\tilde{u}_{\mathrm{ref}}$ (bottom row) at five streamwise locations ($\langle Re_{\mathcal{S}}\rangle \approx 10,595$). Solid lines: present LES; dashed lines: LES by Peller and Manhart; dotted lines: LES by Breuer et al. [14]; dots: LES by Temmerman and Leschziner [12].

The mean wall-normal velocity component $\langle\tilde{w}\rangle/\tilde{u}_{\mathrm{ref}}$ (Fig. 9b) is small in most of the computational domain. Shortly before the hill, the fluid is deflected in the z direction, causing positive wall-normal velocities. The maximum vertical velocity is located just upstream of the hillcrest, at $x \approx 8.5$. The region in which the wall-normal velocity is strongly affected by the cross-sectional narrowing is confined to approximately one hill height above this maximum in the vertical direction. Above that, the effect of the lower-wall contour is rather small. Also note that the zone of high vertical velocity "detaches" from the windward side of the hill. The points just above the hilltop lie in the lee of the hill and are thus not directly influenced by the high velocities upstream.

The contours of the normalized mean density $\langle\bar{\rho}\rangle/\bar{\rho}_{\mathrm{ref}}$ (with the reference density $\bar{\rho}_{\mathrm{ref}} := \langle\bar{\rho}_{\mathcal{S}}\rangle$) in Fig. 9c confirm that our Mach number of $Ma = 0.2$ is sufficiently low to justify a comparison with incompressible reference data. The density is rather uniform in most of the computational domain. Larger deviations from the reference value of unity are confined to small regions at the walls, especially at the lower wall in the postreattachment zone, where the density rises by as much as 7%. This increase of density could cause the deviations that were observed in Sec. IV.C for the Reynolds stresses in this region. As detailed above, the local increase of density is due to an adverse pressure gradient, forcing the upper-wall boundary layer to grow, and leading to moderate density levels of about 1.04 appear

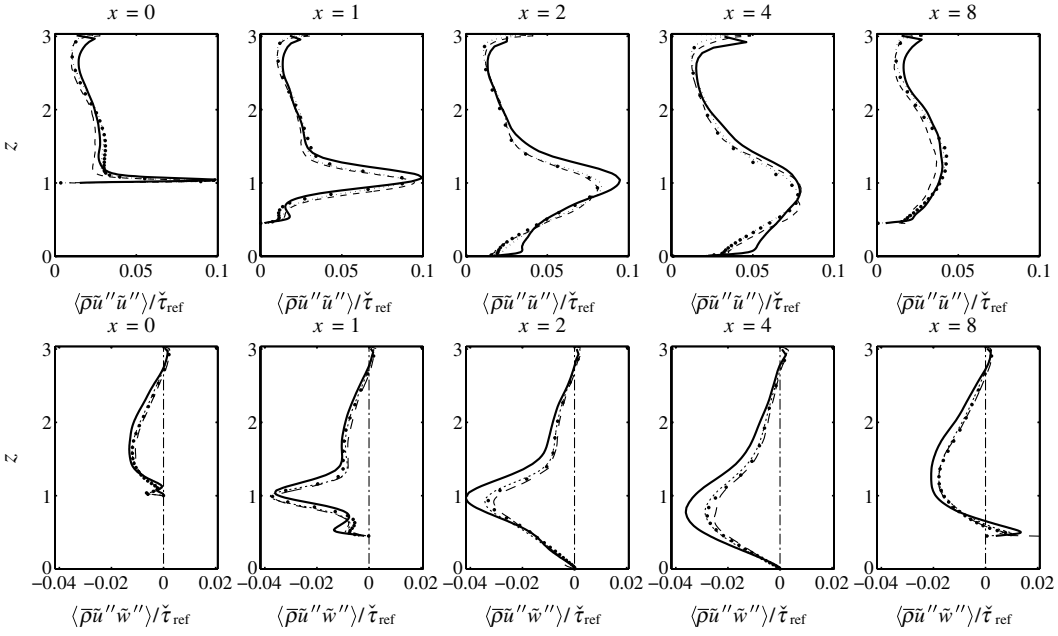

Fig. 8 Profiles of the normalized Reynolds stresses $\langle\bar{\rho}\tilde{u}''\tilde{u}''\rangle/\breve{\tau}_{\mathrm{ref}}$ (top row) and $\langle\bar{\rho}\tilde{u}''\tilde{w}''\rangle/\breve{\tau}_{\mathrm{ref}}$ (bottom row) at five streamwise locations ($\langle Re_{\mathcal{S}}\rangle \approx 10,595$). Solid lines: present LES; dashed lines: LES by Peller and Manhart; dotted lines: LES by Breuer et al. [14]; dots: LES by Temmerman and Leschziner [12].

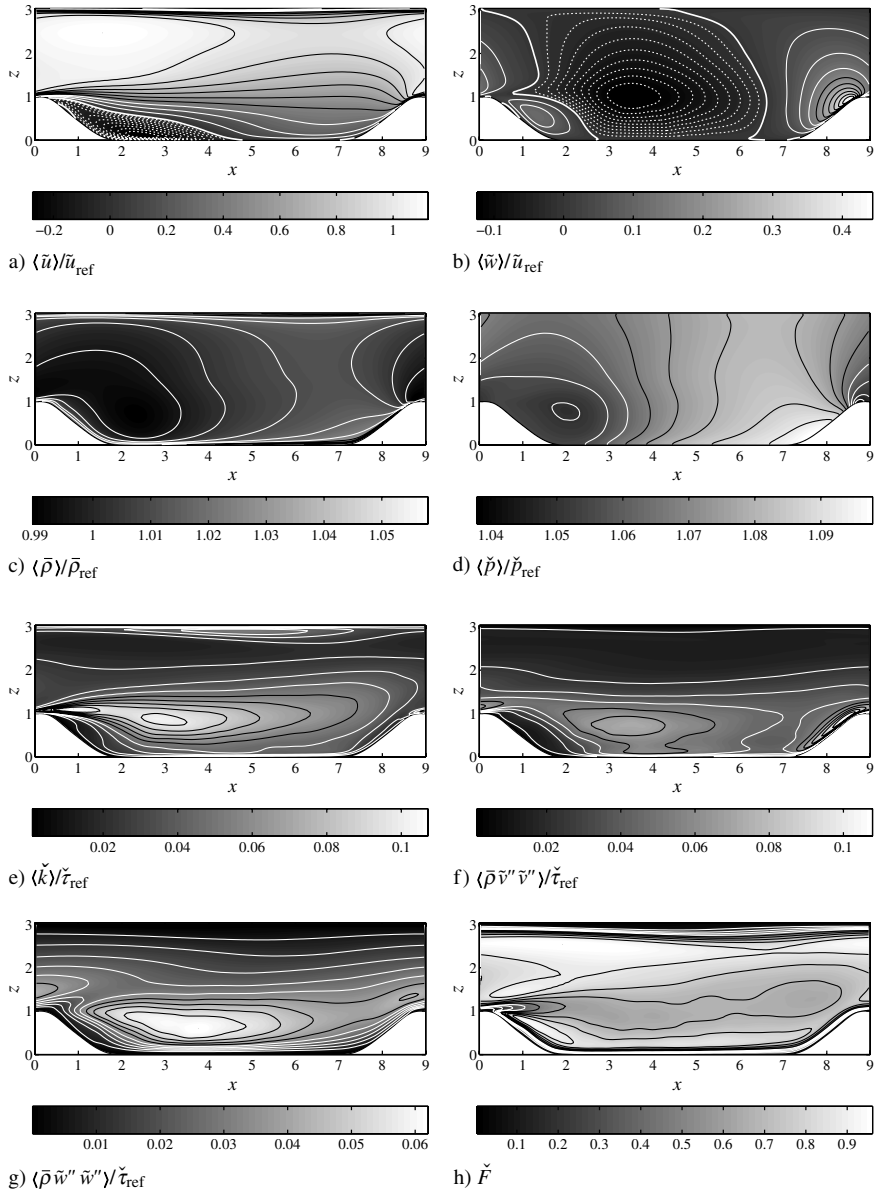

Fig. 9 Contours of normalized mean-flow quantities ($\langle Re_S\rangle \approx 2800$). a) Streamwise velocity $\langle\tilde{u}\rangle/\tilde{u}_{\mathrm{ref}}$; b) wall-normal velocity $\langle\tilde{w}\rangle/\tilde{u}_{\mathrm{ref}}$; c) density $\langle\bar{\rho}\rangle/\bar{\rho}_{\mathrm{ref}}$; d) pressure $\langle\bar{p}\rangle/\bar{p}_{\mathrm{ref}}$; e) turbulent kinetic energy $\langle\bar{k}\rangle/\check{\tau}_{\mathrm{ref}}$; f) spanwise Reynolds stresses $\langle\bar{\rho}\tilde{v}''\tilde{v}''\rangle/\check{\tau}_{\mathrm{ref}}$; g) wall-normal Reynolds stresses $\langle\bar{\rho}\tilde{w}''\tilde{w}''\rangle/\check{\tau}_{\mathrm{ref}}$; and h) Lumley's flatness parameter $\check{F}$ [32]. The dashed lines denote nine evenly distributed negative contour values (i.e., 10 contour intervals) from the global minimum (see corresponding legend) to zero. Similarly, the solid lines symbolize nine evenly distributed positive contour values from zero to the global maximum. The thick solid line is the contour line with a value of zero. If the minimum and maximum are of the same sign, then nine equidistant contour lines between minimum and maximum are shown.

even one hill height away from the walls at $x \approx 7$. The lowest density values are located in the center of the mean-flow recirculation region and the zone of high velocities above the hillcrest.

Figure 9d displays the normalized mean periodic pressure $\langle\check{p}\rangle/\check{p}_{\mathrm{ref}}$ with the reference pressure $\check{p}_{\mathrm{ref}} := 1/\gamma Ma^2$ (i.e., without the contribution of the driving pressure gradient represented by the forcing term). As expected, minimum values are observed in the center of the mean-flow separation region and the region of high-velocity magnitude over the hillcrest. As already observed for the streamwise velocity, the deceleration and accompanying pressure increase extends over a relatively long streamwise stretch downstream of the hill, while the acceleration and pressure drop occur in a much shorter zone. The maximum pressure is observed in the stagnationlike region around the foot of the windward hillside, with a peak a short distance downstream of the separation bubble (cf. Fig. 4b).

The contours of the Reynolds stresses $\langle\bar{\rho}\tilde{u}_i''\tilde{u}_j''\rangle/\check{\tau}_{\mathrm{ref}}$ in Figs. 9e–9g illustrate some of the turbulence properties associated with the separation process. The streamwise Reynolds stresses $\langle\bar{\rho}\tilde{u}''\tilde{u}''\rangle/\check{\tau}_{\mathrm{ref}}$ exhibit high levels in an elongated flat region downstream of the mean separation point due to the vortex shedding and the induced detached shear layer. Although the main recirculation zone only extends to about $x \approx 5$ (Fig. 3), the intensity of the streamwise Reynolds stresses diminishes only slowly and remains quite high until a short distance upstream of the windward hillside. As will be illustrated in the visualization of the instantaneous flow structures in Sec. IV.G, the vortices shed from the hilltop are convected downstream nearly horizontally up to the next hill. The increased stress level within $3 \lesssim x \lesssim 6.5$ along the upper wall goes along with the local thickening of the boundary layer induced by the streamwise-positive pressure gradient.

The spanwise Reynolds stresses $\langle\bar{\rho}\tilde{v}''\tilde{v}''\rangle/\check{\tau}_{\mathrm{ref}}$ shown in Fig. 9f illustrate the region of strong turbulent spanwise mixing. Near the upper wall, the flow is more or less unperturbed by the vortex shedding and mutual vortex interactions. Consequently, the spanwise Reynolds-stress levels are rather small, as in a plane channel. The Reynolds stresses remain small in the upper half of the channel but rise due to the increased proximity of the shear layer.

The horizontal layering of the Reynolds stresses is remarkable and is connected to the nearly horizontal convection of the majority of vortical structures. The high stress levels in the middle of the windward side of the hill can be explained by an enhancement of streamwise vortices by stretching due to flow acceleration, and the impingement of streamwise vortices onto the wall. This "splatting," which was already investigated by Fröhlich et al. [13], induces high spanwise velocity fluctuations, giving rise to an increased level of spanwise stresses. The "blob" of augmented spanwise Reynolds stresses centered at $x \approx 3.5$ is probably caused by the mutual interaction of spanwise- and streamwise-oriented vortices and flow deceleration. Additionally, the vortices shed from the hill need some time to fully develop, leading to a spatial delay in the Reynolds-stress level. Just above the leeward side of the hill, the spanwise stresses are low. This can also be connected to the vortex structures. An animation shows that the vortices are separated shortly after the hillcrest and are convected in the streamwise direction. Although most of the flow structures continue to move mainly horizontally, some recirculate, now moving toward the otherwise protected leeward side of the hill. They are, however, attenuated by dissipation and interaction with the vortices moving in the main flow direction and cannot cause high stress levels near the leeward side of the hill.

The wall-normal Reynolds stresses $\langle \bar{\rho}\tilde{w}''\tilde{w}''\rangle/\check{\tau}_{\mathrm{ref}}$ (Fig. 9g) are low near the walls, and exhibit large values in the mean separation bubble and the acceleration zone on the windward side of the hill. Note that the maximum value of wall-normal stresses is located to the right of and lower than that of the streamwise stresses. This can be explained by the slightly different mechanisms beyond those high stress levels. The latter are caused by the shearing induced by the shedding from the wall. Consequently the streamwise stresses are already large just downstream of the hillcrest. The former, however, are caused by the interaction of vortices, which are convected slightly toward the bottom wall after shedding, thus large values of $\langle \bar{\rho}\tilde{w}''\tilde{w}''\rangle/\check{\tau}_{\mathrm{ref}}$ occur further downstream and closer to the bottom wall.

E. Temporal Spectra of the Velocity Fluctuations

The left column of Fig. 10 displays the power spectra of the three velocity-fluctuation components at five positions a)–e). The power spectra were computed by averaging the spectra of 10 overlapping segments of a continuous time series comprising 45,800 samples. All segments were filtered with a Hann window function $w_{\mathrm{Hann}}(n) = 1/2(1-\cos((2\pi n)/(N-1)))$ to account for nonperiodicity (N denotes the number of samples). Furthermore, the average values of the time series were subtracted before windowing to avoid errors from the interaction of the windowing function with the zero mode. Additionally, the coherent power gain (CPG) for the Hann window

$$\mathrm{CPG} := \sum_{n=0}^{N-1} w_{\mathrm{Hann}}(n)/N \approx 0.5$$

due to the application of the windowing function was corrected for in the resulting spectrum. All spectra exhibit a similar general appearance: roughly an algebraic decay with slope $-5/3$ (which is typical for the inertial subrange) over 1 order of magnitude from Strouhal numbers $St = fh/\tilde{u}_y$ of about 0.1 to 1. For higher frequencies, the power density falls fast and reaches machine accuracy at Strouhal numbers of about 10. Toward the low frequencies, the spectra grow slower or stagnate with different dominant components depending on the cross-sectional position and the Mach number. Note that a distinct inertial subrange is not expected to appear at this low Reynolds number, thus the slope of $-5/3$ is plotted merely for comparison. Even at an almost 4 times higher Reynolds number of $\langle Re_S\rangle \approx 10,595$ [13], a distinct decay with slope $-5/3$ occurs in a frequency range spanning only 1 order of magnitude.

We now consider the differences in energy content for the low-frequency range between the different positions. Figure 10a lies over the hillcrest at a distance of 0.1 from the wall. Here the streamwise ($\tilde{u}$) velocity component is dominant, and the spectra of the spanwise ($\tilde{v}$) and vertical ($\tilde{w}$) velocity components lie about 1 order of magnitude below. This is in contrast to the observations at Fig. 10b, which is roughly in the center of the mean-flow separation bubble. Here the modes of the spectra for the $\tilde{u}$ and $\tilde{v}$ velocities have the largest amplitude in the low-frequency range, while the spectrum for the vertical velocity $\tilde{w}$ lies more than 1 order of magnitude below. Figure 10c is located in the shear layer downstream of the hilltop. In the corresponding power spectra the modes of all three velocity components are close to each other. In the flow-recovery zone in Fig. 10d the modes of the $\tilde{u}$ and $\tilde{v}$ velocities exhibit similar amplitude, whereas the spectrum of the wall-normal velocity $\tilde{w}$ lies more than 1 order of magnitude below. Finally, Fig. 10e is located near the wall approximately halfway up along the windward hillside. Here, the mentioned vortex splatting takes place where vortices shed from the hillcrest impinge onto the windward hill face. This results in high spanwise velocity fluctuations, which are evident, for instance, from the spanwise Reynolds stresses (see Fig. 9f). This impingement process shows in the power spectra of the velocities as the dominance of the $\tilde{v}$ energy density, which lies considerably above the levels observed for the $\tilde{u}$ and $\tilde{w}$ modes. Note that the spectra for the $\tilde{u}$ and $\tilde{w}$ velocities are very similar in shape and magnitude. They are coupled due to the inclination of the windward hillside. Additionally shown in Fig. 10e are the spectra of the wall-parallel and the wall-normal velocity components $\tilde{u}_{\parallel}$ and $\tilde{w}_{\perp}$. Fluctuations of the velocity vector at this position can be mainly attributed to the streamwise component (cf. Figs. 9e–9g). This is also evident from the spectrum of the $\tilde{u}_{\parallel}$ component, which lies somewhat above the one for $\tilde{u}$, while retaining its shape. Consequently, the spectrum of the wall-normal velocity component $\tilde{w}_{\perp}$ is much lower than its $\tilde{w}$ counterpart and all other observed spectra by several orders of magnitude.

F. Turbulence Characteristics

Lumley's flatness parameter [32] $\check{F}(x,z) := 1 + 9\check{I}I(x,z) + 27\check{I}\check{I}I(x,z)$ allows for an analysis of the turbulence characteristics of the flow. It is computed from the two invariants $-\check{I}I := 1/2\check{b}_{ij}\check{b}_{ji}$ and $\check{I}\check{I}I := 1/3\check{b}_{ij}\check{b}_{jk}\check{b}_{ki}$ of the normalized anisotropy tensor $\check{b}_{ij} := \langle \bar{\rho}\tilde{u}_i''\tilde{u}_i''\rangle/\langle \bar{\rho}\tilde{u}_k''\tilde{u}_k''\rangle - 1/3\delta_{ij}$ and varies between 0 and 1. A very small value of $\check{F}$ denotes two-component turbulence characteristics, as typical, for instance, in a turbulent boundary layer, whereas a value near 1 evidences three-component (isotropic) turbulence structure. As expected, the values of $\check{F}$ in Fig. 9h are very small in the boundary layers at the lower and upper walls. The thickening of the upper-wall boundary layer can be well observed. Near the lower wall, two-component turbulence is also prevalent in the shear layer downstream of the hillcrest, whose characteristics are only gradually displaced by that of the surrounding flow.

Although $\check{F}$ reaches values that are very close to zero, that is, two-component turbulence, its maximum of $\check{F}_{\max} \approx 0.95$ lies somewhat below the value for three-component turbulence, $\check{F} = 1$. This result is typical for channel flow and can be explained by the nature of the flow configuration and the low Reynolds number. The specific geometry, including the separated boundary-layer downstream of the hill as well as the influence of the upper and lower walls, does not allow for the development of full three-component isotropic turbulence. On the other hand, in wall-bounded turbulence two-component turbulence characteristics are enforced by the presence of solid walls. However, high values of $\check{F}$ are present in the whole upper channel part between the upper-wall boundary layer and the shear layer ($z > 1$), and in the lower channel part ($z < 1$) between the lower-wall boundary layer and the shear layer. The very highest $\check{F}$ values with almost full three-component turbulence are visible in distinct elongated patches lying in the high-velocity region above the leeward hill face close to the upper wall.

A more detailed insight into the local turbulence structure can be gained from Lumley's realizability maps [32] ("Lumley's triangle"). For each point in the flow, the two invariants $-\check{I}I$ and $\check{I}\check{I}I$ of the normalized anisotropy tensor are displayed in a parameter chart. The location in this diagram and specifically the proximity to the bounding curves of the triangle characterizes the nature of the

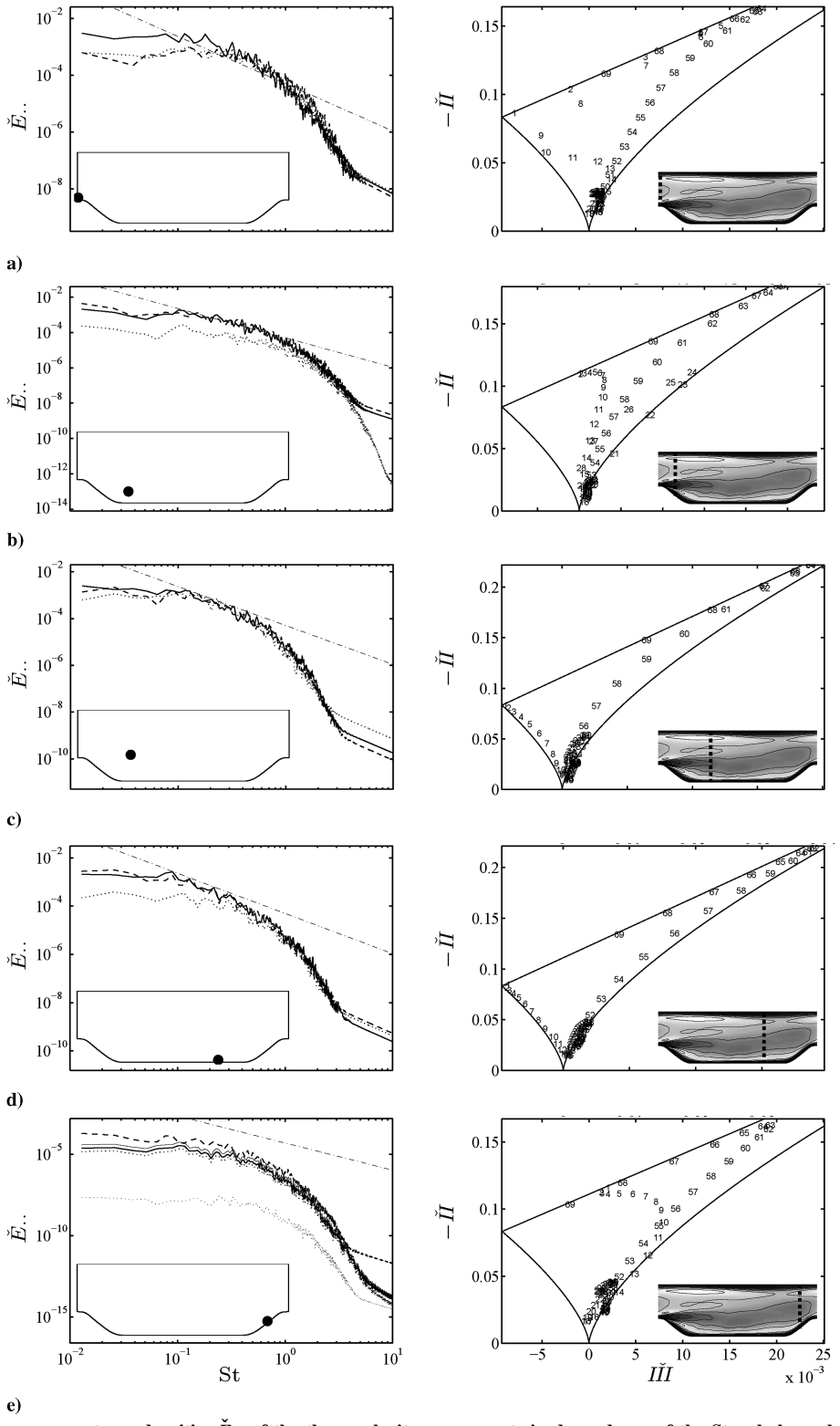

Fig. 10 Left column: power spectrum densities $\check{E}..$ of the three velocity components in dependence of the Strouhal number $St = fh/\tilde{u}_{\mathcal{V}}$ (with the frequency f) at several locations a)–e), marked by the dots in the inset sketches ($\langle Re_{\mathcal{S}} \rangle \approx 2800$). Solid lines: $\check{E}_{\tilde{u}\tilde{u}}$; dashed lines: $\check{E}_{\tilde{v}\tilde{v}}$; dotted lines: $\check{E}_{\tilde{w}\tilde{w}}$; dash-dotted lines: slope −5/3. Additionally shown in panel e): spectra of the wall-parallel velocity component $\tilde{u}_{\parallel}$ (thin solid line) and the wall-normal velocity component $\tilde{w}_{\perp}$ (thin dotted line). Right column: Lumley's anisotropy invariant triangle for five vertical lines a)–e) as indicated by the thick dashed lines in the inset sketches ($\langle Re_{\mathcal{S}} \rangle \approx 2800$). The numbers in the Lumley triangles correspond to the positions along the lines, that is, the positions within the channel. The lowest numbers are located close to the bottom wall and the highest numbers near the top wall.

turbulence at this point. The bottom corner ($\check{I}\check{I}\check{I} = 0, -\check{I}\check{I} = 0$) of the triangle denotes three-component isotropic turbulence, while the left corner stands for two-component axisymmetric turbulence structure. In the right corner of the triangle, one-component turbulence prevails. Along the left bounding curve axisymmetric contraction takes place, whereas the right bounding curve represents axisymmetric expansion. The upper bounding curve denotes two-component turbulence.

In the right column of Fig. 10 we display the trajectories through Lumley's triangle for points along five vertical lines with constant

streamwise coordinates ($x = 0, 1, 3, 6, 8$). In Fig. 10a, the turbulence structure is 2-D axisymmetric directly above the hillcrest. The trajectory then follows the two-component boundary, until it returns to the axisymmetric-contraction line and approaches the range of three-component isotropic turbulence, where it stays for the majority of the remaining positions. A comparison with the contour visualization of the flatness parameter $\check{F}$ in Fig. 10 reveals that those positions span the complete vertical distance from the separating lower-wall boundary layer up to the upper-wall boundary layer. When approaching the top wall, the turbulence structure changes from the three-component state in the interior to a two-component one. In Lumley's triangle, this results in a movement roughly near the axisymmetric-expansion boundary toward the corner denoting one-component turbulence. For the last few mesh points below the upper wall, the turbulence state moves along the two-component line toward the 2-D axisymmetric corner where the trajectory starts at the lower wall.

In Fig. 10b at $x = 1$, the noteworthy features of the invariant trajectories are due to the shear layer downstream of the hillcrest and the specific turbulence characteristics of the upper-wall boundary layer in this highly accelerated flow region. The turbulence at the leeward hillside exhibits a two-component state. As the positions cut through the secondary separation bubble, the trajectory traverses the interior of the triangle toward the corner marking 3-D isotropic turbulence. In the next stretch along the line, the turbulence characteristics remain close to 3-D isotropic, until the vertical position of the separated boundary layer is reached. In this rather thin shear layer the trajectory shows a strong spike along the 2-D expansion boundary and returns back to a nearby 3-D isotropic state at the upper edge of the shear layer. The following development of the trajectory for increasing z coordinates strongly resembles the observations for the previous position (Fig. 10a) above the hillcrest. The turbulence state changes roughly along the axisymmetric-expansion boundary toward the corner of one-component turbulence and returns along the two-component line toward the two-component axisymmetric state.

Figure 10c at $x = 3$ is interesting because it cuts through the mean-flow recirculation region. The initial turbulence structure is 2-D axisymmetric. When moving away from the lower wall, the trajectory follows the axisymmetric-contraction boundary toward a 3-D isotropic state, which is reached after a relatively short distance. In the complete interior of the channel, the trajectory moves back and forth near the 3-D isotropic limit. Close to the upper wall, the turbulence structure changes along the axisymmetric-expansion curve and approaches the one-component state rather closely. Only for positions very close to the upper wall, a second Reynolds-stress component gains importance and the trajectory departs from the 1-D corner along the two-component boundary.

At $x = 6$, denoted by Fig. 10d, the trajectory looks very similar to the one at the previous position. However, in contrast to Fig. 10c, the 3-D isotropic state is not reached as closely here, and the trajectory returns along the two-component boundary at a position which is considerably farther away from the one-component limit. On the other hand, the turbulence at the upper wall comes closer to a 2-D axisymmetric state than observed farther upstream.

Figure 10e at $x = 8$ is located in the flow acceleration region on the upstream hillside. For positions halfway up the windward hill face, the trajectory starts at the two-component limit, then moves into the interior of the triangle and bends to align with the axisymmetric-expansion boundary. In the major part of the channel cross section, the flow exhibits primarily 3-D isotropic characteristics. Only when approaching the upper wall, the turbulence state moves along the axisymmetric-expansion line toward the corner denoting one-component turbulence. Directly at the wall it returns back along the two-component line approximately to its starting point from the lower wall.

G. Instantaneous Flowfield and Separation Characteristics

Previous studies of transitional flows [26,45] demonstrated that it is well possible for LES to reproduce complex vortical flow structures of a DNS accurately, within the limits of the employed resolution. In the following we illustrate the major instantaneous flow features of our LES at Reynolds number $\langle Re_S \rangle \approx 2800$ with the $\check{\lambda}_2$ vortex-identification criterion [46]. An animation of the isosurfaces of $\check{\lambda}_2$ allows the identification of several effects associated with the vortices shed from the hilltop while traveling downstream. On their way to the windward hill face, they interact mutually and with the surrounding flowfield, which results in a change of their orientation, strength, or shape. Figure 11 shows four characteristic snapshots of the instantaneous isosurfaces $\check{\lambda}_2 = -8$. Note that the upper two and the lower two pictures represent a distinct series, with the right picture taken a few time steps after the left one.

At first glance, the abundance of vortical structures upstream of the mean reattachment zone is in contrast to their relative sparsity further downstream. Although most vortices are mainly oriented in the streamwise direction, some differences are observable. Because of a Kelvin–Helmholtz shear instability [13], spanwise rollers (e.g., the structure marked with a circled 1 in Fig. 11a) are generated in the region of the mean separation line. Those elongated structures can span several hill heights h in the spanwise direction, as does vortex 2 in Fig. 11a (continued on the other side of the periodic domain). The need for a large spanwise domain width to obtain sufficient spanwise decorrelation (and thus no unphysical truncation of the homogeneous spanwise boundaries) is in large part determined by the horizontal extent of such vortices. Fröhlich et al. [13] showed in a test calculation with a spanwise box size of $L_y = 9$ that the velocity autocorrelations would vanish satisfactorily for $L_y \gtrsim 7$, but refrained from using this value due to computational cost. Additionally, the sensitivity of the results to the spanwise box size was found to be rather small between $L_y = 4.5$ and $L_y = 9$.

Shortly after separation, the ends of some spanwise rollers are bent forward and upward (in the positive z direction), yielding a V-shaped vortex (see vortices 1 and 2 in Fig. 11b or vortex 3 in Figs. 11c and 11d). Because of the higher streamwise velocity in the elevated arms than in the lower spanwise vortex part and due to interference of other vortices, most V-shaped vortices are stretched and break up into two longitudinal vortices shortly thereafter. The bending of the vortex ends could be associated with the interaction with streamwise vortices and streaky structures on the hillcrest, as indicated by the vortices marked 4 in Figs. 11a and 11b.

A change of orientation is also observable for the streamwise vortices, leading to their inclination toward the upper wall (see, e.g., structure 5 in Figs. 11a and 11b). Near the windward side of the hill, the longitudinal vortices are strongly stretched due to the flow acceleration, as apparent for vortex 6 in Figs. 11c and 11d. This causes an increase of the local vorticity and stresses in this region, as seen in the corresponding contour plots of the turbulent kinetic energy and the Reynolds stresses in Fig. 9. Also visible in an animation of $\check{\lambda}_2$ is the impingement (splatting) of longitudinal vortices onto the windward hill face, which was investigated in some detail by Fröhlich et al. [13].

Furthermore, notice in Figs. 11a–11d the constant presence of a flat, nearly two-dimensional and rather stationary region of constant $\check{\lambda}_2$, covering the whole windward-oriented hilltop in the spanwise direction. However, as apparent in Figs. 11a and 11b near marker 4, streamwise vortices crossing the hillcrest are able to disturb the otherwise fairly homogeneous zone, which is probably an artifact of $\check{\lambda}_2$ due to the near-wall pressure minimum at the velocity peak. On rarer occasions, it is possible to witness the creation of small streamwise vortices (attributed to Görtler instabilities by Fröhlich et al. [13]) at the foot of the windward hillside; see, for example, the vortex marked by 7.

H. Backflow at the Walls

As apparent from the visualizations of the instantaneous flowfield in Figs. 12a and 12b, there is considerable backflow along the walls at all times. To better quantify this phenomenon, we analyzed the time

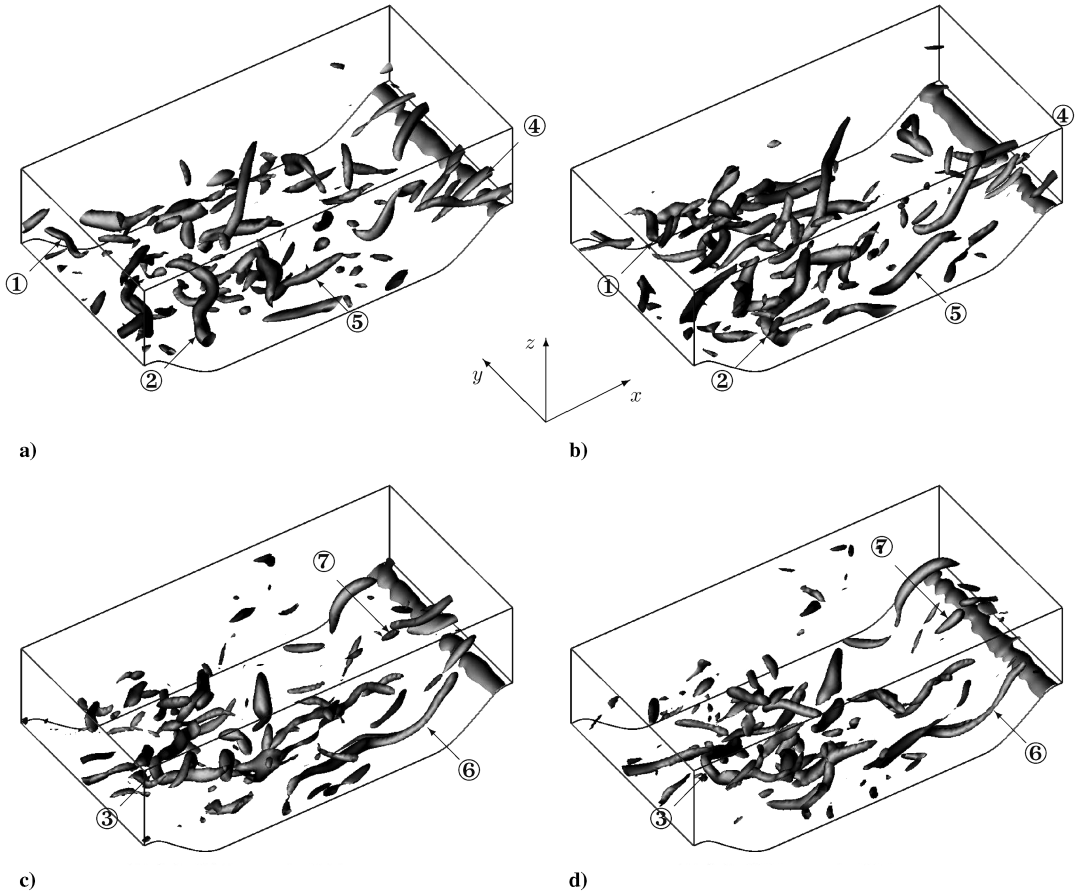

Fig. 11 Isosurfaces of the vortex-identification measure $\check{\lambda}_2 = -8$ [46] at 4 times. The upper two and lower two pictures represent a separate series. Flow direction is from left to right ($\langle Re_S \rangle \approx 2800$).

fraction r at which the wall-parallel velocity $\tilde{u}_\parallel := \tilde{\boldsymbol{u}} \cdot \boldsymbol{t}_{\text{wall}}$ close to the wall is negative, that is,

$$r(x) = \frac{1}{L_y} \int_{y=0}^{L_y} \frac{1}{\Delta T} \int_{t=t_0}^{t_0+\Delta T} [1 - \text{Heaviside}(\tilde{u}_\parallel(x, y, t))] \, \mathrm{d}t \, \mathrm{d}y \quad (2)$$

We used the first cell off the wall for the determination of $\tilde{u}_\parallel$ (see Sec. III for information about the dimensionless wall distance). Alternatively, the friction coefficient c_f could be used in Eq. (2) instead of the wall-parallel velocity. In the above equation, $\boldsymbol{t}_{\text{wall}}$ denotes the wall-tangent vector in positive x direction and ΔT a sufficiently long time-integration interval. The result is displayed in Fig. 12c.

At the lower wall, the flow acceleration and the resulting high velocities above the hillcrest prevent backflow, thus r is essentially zero. Just downstream of the hillcrest, the flow separates and vortices are shed, yielding a sharply rising backflow fraction with a peak of more than 70%. This location lies just downstream of the mean-flow separation point and exhibits the second-largest magnitude of backflow along the bottom wall. Because of the secondary recirculation zone with opposite orientation, which is embedded in the main separation bubble, r is then decreasing rapidly to about 25%. The backflow fraction grows again at a slower rate downstream of this secondary separation region. Here a little local maximum appears in the strongly curved region at the leeside foot of the hill. Downstream of that dent, r increases again to a global maximum of almost 100%, which is located near the streamwise coordinate of the center of the primary mean-flow separation bubble. Downstream of this maximum, the backflow ratio decreases moderately until it reaches a plateau near the mean-flow reattachment location.

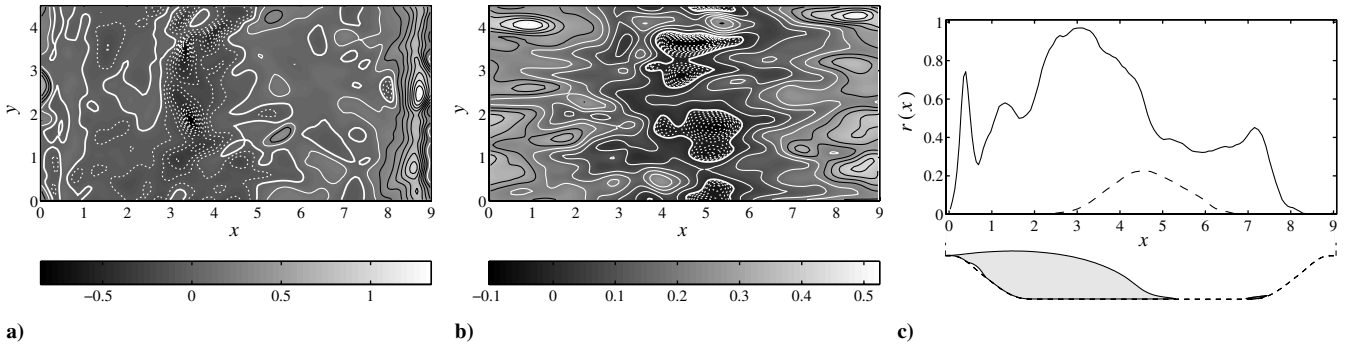

Fig. 12 Visualization of the instantaneous wall-parallel velocity $\tilde{u}_\parallel$ at a) top wall and b) bottom wall (legend of contour lines as in Fig. 9). c) Fraction of backflow r at lower wall (solid line) and upper wall (dashed line) at $\langle Re_S \rangle \approx 2800$. Sketch below: primary mean-flow separation region (shaded in gray) and domain boundaries (dashed line).

The backflow ratio remains at levels between 40% and 50% in the flow-recovery region, until it grows again somewhat due to the small separation bubble at the windward hill foot. Farther downstream, the flow accelerates strongly and the ratio of backflow falls rapidly. Along the second half of the windward hill face ($z > 0.5$) the backflow rate is negligible. Also note the kink of the graph at the end of the curved region of the hill foot ($x \approx 8$), which is potentially due to wall-curvature effects or the previously mentioned vortex splatting against the windward hill face. At the upper wall the backflow rates are considerably smaller. Significant backflow of up to 25% only occurs within $3 \leq x \leq 6$ due to the adverse pressure gradient, which is also responsible for the thickening of the boundary layer in this region.

V. Conclusions

Large-eddy simulations using the approximate-deconvolution subgrid-scale model of the unsteady separated flow in a channel with streamwise-periodic constrictions have been performed at two Reynolds numbers of 2800 and 10,595. Because of the low Mach number of 0.2, selected for comparison with incompressible flow data, compressibility effects were found to be small as expected, except for two small regions near the lower and upper walls upstream of the hill.

To reduce the simulation effort and to demonstrate the ability of LES using ADM to yield quantitatively accurate results at relatively low computational cost, the spatial resolution has been chosen near the lower limit for this flow configuration and parameters. Nevertheless, our results show good agreement for most quantities and streamwise positions. Vertical profiles of the first- and second-order statistics have been presented and compared to incompressible direct numerical simulation data at the lower Reynolds number, as well as to high-resolution LES data at the higher one. The separation and reattachment locations of the mean flow, as well as the friction and pressure coefficients at the lower wall, are predicted in good agreement with the reference data.

The main features of the mean flow were pointed out by means of spanwise contour plots. We analyzed the frequency content of the velocity fluctuations and their dominant components by studying their energy density spectra and investigated the local turbulence structure in detail with Lumley's flatness parameter and anisotropy triangle. We introduced a new measure quantifying the backflow along the walls and illustrated the instantaneous flowfield and some mechanisms of the vortex shedding process by visualizing the vortex structures with the $\check{\lambda}_2$ vortex-identification criterion.

The streamwise-periodic hill channel configuration has proven to be a challenging and computationally expensive test case, especially due to the need of a minimum (in particular, streamwise) resolution of the separation and reattachment zones, a large spanwise box size due to the presence of elongated spanwise vortical structures, the necessary long statistical sampling time, and the small time steps associated with the low Mach number of 0.2.

Acknowledgments

We are grateful to N. Peller, M. Manhart, and M. Breuer for generously sharing their data. We would like to thank P. Schlatter, J. Vos, and D. Obrist for fruitful discussions. Calculations have been performed on the NEC SX-5 at the Swiss National Supercomputing Centre (CSCS).

References

[1] Temmerman, L., Leschziner, M. A., Mellen, C. P., and Fröhlich, J., "Investigation of Wall-Function Approximations and Subgrid-Scale Models in Large Eddy Simulation of Separated Flow in a Channel with Streamwise Periodic Constrictions," *International Journal of Heat and Fluid Flow*, Vol. 24, No. 2, 2003, pp. 157–180. doi:10.1016/S0142-727X(02)00222-9

[2] Manceau, R., and Bonnet, J.-P., *Proceedings of the 10th ERCOFTAC/IAHR/QNET-CFD Workshop on Refined Turbulence Modelling*, Laboratoire d'études Aerodynamiques, UMR CNRS 6609, Université de Poitiers, France, 2003.

[3] Sagaut, P., *Large Eddy Simulation for Incompressible Flows: An Introduction*, 3rd ed., Springer–Verlag, New York, 2005.

[4] Meneveau, C., and Katz, J., "Scale-Invariance and Turbulence Models for Large-Eddy Simulation," *Annual Review of Fluid Mechanics*, Vol. 32, No. 1, 2000, pp. 1–32. doi:10.1146/annurev.fluid.32.1.1

[5] Lesieur, M., and Métais, O., "New Trends in Large-Eddy Simulations of Turbulence," *Annual Review of Fluid Mechanics*, Vol. 28, Jan. 1996, pp. 45–82. doi:10.1146/annurev.fl.28.010196.000401

[6] Domaradzki, J. A., and Adams, N. A., "Direct Modelling of Subgrid Scales of Turbulence in Large-Eddy Simulations," *Journal of Turbulence*, Vol. 3, N24, April 2002, pp. 1–19. doi:10.1088/1468-5248/3/1/024

[7] Almeida, G. P., Durão, D. F. G., and Heitor, M. V., "Wake Flows Behind Two-Dimensional Model Hills," *Experimental Thermal and Fluid Science*, Vol. 7, No. 1, 1993, pp. 87–101. doi:10.1016/0894-1777(93)90083-U

[8] Jang, Y. J., Temmerman, L., and Leschziner, M. A., "Investigation of Anisotropy-Resolving Turbulence Models by Reference to Highly-Resolved LES Data for Separated Flow," *European Congress on Computational Methods in Applied Sciences and Engineering 2001, Swansea, Wales*, [CD-ROM], European Community on Computational Methods in Applied Sciences, 4–7 Sept. 2001, pp. 4–7.

[9] Jang, Y. J., Leschziner, M. A., Abe, K., and Temmerman, L., "Investigation of Anisotropy-Resolving Turbulence Models by Reference to Highly-Resolved LES Data for Separated Flow," *Flow, Turbulence and Combustion*, Vol. 69, No. 9, Nov. 2002, pp. 161–203. doi:10.1023/A:1024764307706

[10] Abe, K., Jang, Y.-J., and Leschziner, M. A., "An Investigation of Wall-Anisotropy Expressions and Length-Scale Equations for Non-Linear Eddy-Viscosity Models," *International Journal of Heat and Fluid Flow*, Vol. 24, No. 2, 2003, pp. 181–198. doi:10.1016/S0142-727X(02)00237-0

[11] Mellen, C. P., Fröhlich, J., and Rodi, W., "Large Eddy Simulation of the Flow over Periodic Hills," *16th IMACS World Congress, Lausanne, Switzerland*, edited by M. Deville, and R. Owens, IMACS, Dept. of Computer Science, Rutgers University, 2000, pp. 21–25, ISBN 3-9522075-1-9.

[12] Temmerman, L., and Leschziner, M. A., "Large Eddy Simulation of Separated Flow in a Streamwise Periodic Channel Constriction," *Turbulence and Shear Flow Phenomena 2*, edited by E. Lindborg, A. Johansson, J. Eaton, J. Humphrey, N. Kasagi, M. Leschziner, and M. Sommerfeld, Taylor & Francis, London, Vol. 3, 2001, pp. 399–404.

[13] Fröhlich, J., Mellen, C. P., Rodi, W., Temmerman, L., and Leschziner, M. A., "Highly Resolved Large-Eddy Simulation of Separated Flow in a Channel with Streamwise Periodic Constrictions," *Journal of Fluid Mechanics*, Vol. 526, Feb. 2005, pp. 19–66. doi:10.1017/S0022112004002812

[14] Breuer, M., Jaffrézic, B., Peller, N., Manhart, M., Fröhlich, J., Hinterberger, C., Rodi, W., Deng, G., Chikhaoui, O., Šarić, S., and Jakirlić, S., "A Comparative Study of the Turbulent Flow Over a Periodic Arrangement of Smoothly Contoured Hills," *Direct and Large-Eddy Simulation VI*, edited by E. Lamballais, R. Friedrich, B. J. Geurts, and O. Métais, Vol. 10, ERCOFTAC Series, Springer Science, Dordrecht, The Netherlands, Sixth International ERCOFTAC Workshop on DNS and LES: DLES-6, Poitiers, France, 12–14 Sept. 2005, 2006, pp. 635–642.

[15] Breuer, M., Peller, N., Rapp, C., and Manhart, M., "Flow over Periodic Hills—Numerical and Experimental Study in a Wide Range of Reynolds Numbers," *Journal of Fluids Engineering* (to be published).

[16] Peller, N., and Manhart, M., "DNS einer Kanalströmung mit periodisch angeordneten Hügeln," *STAB (Arbeitsgemeinschaft "Strömung mit Ablösung") Jahresbericht 2004*, 14. DGLR/STAB Fachsymposium, Bremen, Germany, [online], 16–18 Nov. 2004, p. 178 f.

[17] Ziefle, J., "Large-Eddy Simulation of Massively Separated Turbulent Flows," Ph.D. Thesis, ETH Zurich, Zurich, Switzerland (in preparation).

[18] Ziefle, J., and Kleiser, L., "Compressibility Effects on Turbulent Separated Flow in a Streamwise-Periodic Hill Channel—Part 1," *IUTAM Symposium on Unsteady Separated Flows and Their Control*, Springer, 18–22 June 2007 (to be published).

[19] Ziefle, J., and Kleiser, L., "Compressibility Effects on Turbulent Separated Flow in a Streamwise-Periodic Hill Channel—Part 2," *Second DESider Symposium on Hybrid RANS-LES Methods*, Notes on Numerical Fluid Mechanics and Multidisciplinary Design, Springer, Berlin, 17–18 June 2007, pp. 316–325, ISBN: 978-3-540-77813-4. doi:10.1007/978-3-540-77815-8

[20] Stolz, S., and Adams, N. A., "An Approximate Deconvolution Procedure for Large-Eddy Simulation," *Physics of Fluids*, Vol. 11, No. 7, 1999, pp. 1699–1701. doi:10.1063/1.869867

[21] Stolz, S., Adams, N. A., and Kleiser, L., "An Approximate Deconvolution Model for Large-Eddy Simulation with Application to Incompressible Wall-Bounded Flows," *Physics of Fluids*, Vol. 13, No. 4, 2001, pp. 997–1015. doi:10.1063/1.1350896

[22] Stolz, S., Adams, N. A., and Kleiser, L., "The Approximate Deconvolution Model for Large-Eddy Simulations of Compressible Flows and its Application to Shock-Turbulent-Boundary-Layer Interaction," *Physics of Fluids*, Vol. 13, No. 10, 2001, pp. 2985–3001. doi:10.1063/1.1397277

[23] Rembold, B., and Kleiser, L., "Noise Prediction from Rectangular Jet Flow Using LES," *AIAA Journal*, Vol. 42, No. 9, 2004, pp. 1823–1831.

[24] Rembold, B., Adams, N. A., and Kleiser, L., "Direct and Large-Eddy Simulation of a Transitional Rectangular Jet," *Direct and Large-Eddy Simulation IV*, edited by B. J. Geurts, R. Friedrich, and O. Métais, Kluwer, Dordrecht, The Netherlands, 2002, pp. 197–204.

[25] Schlatter, P., Stolz, S., and Kleiser, L., "LES of Transitional Flows Using the Approximate Deconvolution Model," *International Journal of Heat and Fluid Flow*, Vol. 25, No. 3, 2004, pp. 549–558. doi:10.1016/j.ijheatfluidflow.2004.02.020

[26] Schlatter, P., "Large-Eddy Simulation of Transition and Turbulence in Wall-Bounded Shear Flow," Ph.D. Thesis, ETH Zurich, Zurich, Switzerland, Dissertation No. 16000, 2005.

[27] von Kaenel, R., Kleiser, L., Adams, N. A., and Vos, J. B., "Effect of Artificial Dissipation on Large-Eddy Simulation with Deconvolution Modeling," *AIAA Journal*, Vol. 41, No. 8, 2003, pp. 1606–1609.

[28] von Kaenel, R., Adams, N. A., Kleiser, L., and Vos, J. B., "The Approximate Deconvolution Model for Large-Eddy Simulation of Compressible Flows with Finite Volume Schemes," *Journal of Fluids Engineering*, Vol. 125, No. 2, March 2003, pp. 375–381. doi:10.1115/1.1567471

[29] von Kaenel, R., Kleiser, L., Adams, N. A., and Vos, J. B., "Large-Eddy Simulation of Shock-Turbulence Interaction," *AIAA Journal*, Vol. 42, No. 12, 2004, pp. 2516–2528.

[30] Ziefle, J., Stolz, S., and Kleiser, L., "Large-Eddy Simulation of Separated Flow in a Channel with Streamwise-Periodic Constrictions," AIAA Paper 2005-5353, 6–9 June 2005.

[31] Ziefle, J., and Kleiser, L., "Large-Eddy Simulation of a Round Jet in Crossflow," AIAA Paper 2006-3370, June 2006.

[32] Lumley, J. L., "Computational Modeling of Turbulent Flows," *Advances in Applied Mechanics*, Vol. 18, Academic Press, New York, 1978, pp. 123–176.

[33] Vos, J. B., van Kemenade, V., Ytterström, A., and Rizzi, A. W., "Parallel NSMB: An Industrialized Aerospace Code for Complete Aircraft Simulations," *Parallel CFD Conference 1996*, edited by P. Schiano, A. Ecer, J. Periaux, and N. Satofuka, North-Holland, Amsterdam, 1997.

[34] Vos, J. B., Rizzi, A., Corjon, A., Chaput, E., and Soinne, E., "Recent Advances in Aerodynamics Inside the NSMB (Navier Stokes Multi Block) Consortium," AIAA Paper 98-0225, 1998.

[35] Vos, J. B., Leyland, P., van Kemenade, V., Gacherieu, C., Duquesne, N., Lotstedt, P., Weber, C., Ytterström, A., and Saint Requier, C., *NSMB Handbook 4.5*.

[36] Gacherieu, C., Collercandy, R., Larrieu, P., Soumillon, P., Tourette, L., and Viala, S., "Navier-Stokes Calculations at Aerospace Matra Airbus for Aircraft Design," *Proceedings of ICAS*, edited by G. I., Royal Aeronautical Society, London, U.K., 2000.

[37] Viala, S., Amant, S., and Tourette, L., "Recent Achievements on Navier-Stokes Methods for Engine Integration," *CEAS Aerospace Aerodynamics Research Conference* [CD-ROM], Royal Aeronautical Society, London, U.K., June 2002, ISBN: 1857681975.

[38] Mossi, M., "Simulation of Benchmark and Industrial Unsteady Compressible Turbulent Fluid Flows," Ph. D. Thesis No. 1958, EPFL, Lausanne, Switzerland, 1999.

[39] Stolz, S., "Large-Eddy Simulation of Complex Shear Flows Using an Approximate Deconvolution Model," Vol. 7/403, Fortschritt-Berichte VDI, Ph.D. Thesis, ETH Zurich, Zurich, Switzerland, VDI Verlag, 2001.

[40] Coleman, G. N., Kim, J., and Moser, R. D., "A Numerical Study of Turbulent Supersonic Isothermal-Wall Channel Flow," *Journal of Fluid Mechanics*, Vol. 305, Dec. 1995, pp. 159–183. doi:10.1017/S0022112095004587

[41] Program Development Company, 300 Hamilton Avenue Suite 409, White Plains, NY 10601, *GridPro v4.1 User's Guide and Reference Manual*, Program Development Company (PDC), 1999.

[42] Blaisdell, G. A., Spyropoulos, E. T., and Qin, J. H., "The Effect of the Formulation of Nonlinear Terms on Aliasing Errors in Spectral Methods," *Applied Numerical Mathematics*, Vol. 21, No. 3, July 1996, pp. 207–219. doi:10.1016/0168-9274(96)00005-0

[43] Nicoud, F., and Ducros, F., "Subgrid-Scale Modeling Based on the Square of the Velocity Gradient Tensor," *Flow, Turbulence and Combustion*, Vol. 62, No. 3, Sept. 1999, pp. 183–200. doi:10.1023/A:1009995426001

[44] Boris, J. P., "Whither Turbulence? Turbulence at the Crossroads," *On Large Eddy Simulation Using Subgrid Turbulence Models*, Springer, New York, 1989, pp. 344–353.

[45] Schlatter, P., Stolz, S., and Kleiser, L., "Applicability of LES Models for Prediction of Transitional Flow Structures," *Laminar-Turbulent Transition*, edited by R. Govindarajan, Sixth IUTAM Symposium, Springer, New York, 2006, pp. 323–328. doi:10.1007/1-4020-4159-4_45

[46] Jeong, J., and Hussain, F., "On the Identification of a Vortex," *Journal of Fluid Mechanics*, Vol. 285, Feb. 1995, pp. 69–94. doi:10.1017/S0022112095000462

P. Givi
Associate Editor